Selective and scalable control of spin quantum memories in a photonic circuit

D. Andrew Golter,[*,†,#] Genevieve Clark,[*,†,‡,#] Tareq El Dandachi,[‡] Stefan Krastanov,[‡] Andrew J. Leenheer,[ǂ] Noel H. Wan,[‡] Hamza Raniwala,[‡] Matthew Zimmermann,[†] Mark Dong,[†,‡] Kevin C. Chen,[‡] Linsen Li,[‡] Matt Eichenfield,[*, ǂ, §] Gerald Gilbert,[*, ⊥] Dirk Englund[*,‡]

[†]*The MITRE Corporation, 202 Burlington Road, Bedford, Massachusetts 01730, USA*
[‡]*Research Laboratory of Electronics, Massachusetts Institute of Technology, Cambridge, Massachusetts 02139, USA*
[ǂ]*Sandia National Laboratories, P.O. Box 5800 Albuquerque, New Mexico 87185, USA*
[§]*College of Optical Sciences, University of Arizona, Tucson, Arizona 85719, USA*
[⊥]*The MITRE Corporation, 200 Forrestal Road, Princeton, New Jersey 08540, USA*
#These authors contributed equally to this work.

Supporting Information

Approved for Public Release; Distribution Unlimited. Public Release Case Number 22-2340

1: Derivation of the exact, closed-form expression for the error function

Here we show the calculation of the exact, closed-form expression for the error function given in Eq. (1), which is defined as

$$\epsilon_j = 1 - \left|\langle 0,1|U_j|0,1\rangle\right|^2 \tag{A1}$$

where the notation means that the matrix element is evaluated either in the ground state or in the excited state (we will see that the value of the error is the same for both). Here U_j is the unitary evolution operator $U_j = \exp(-iH_j t/\hbar)$ for the spin at location j, where H_j is the local Hamiltonian. We begin by deriving some useful identities associated with the Hamiltonian of the system. The Hamiltonian operator associated with the j^{th} spin site is given by

$$\begin{aligned} H_j &= \frac{\hbar}{2}\{\Delta_j\sigma_z + \Omega_0[\cos(\varphi_j)\sigma_x + \sin(\varphi_j)\,\sigma_y]\} \\ &= \frac{\hbar\Delta_j}{2}\begin{pmatrix} 1 & \frac{\Omega_0}{\Delta_j}e^{-i\varphi_j} \\ \frac{\Omega_0}{\Delta_j}e^{i\varphi_j} & -1 \end{pmatrix} \\ &= \frac{\hbar\Delta_j}{2}\begin{pmatrix} 1 & x_j e^{-i\varphi_j} \\ x_j e^{i\varphi_j} & -1 \end{pmatrix}, \end{aligned} \tag{A2}$$

where $x_j \equiv \Omega_0/\Delta_j$, Ω_0 is the Rabi frequency, Δ_j is the detuning frequency associated to the j^{th} spin, φ_j is the phase associated to the j^{th} spin, and σ_x, σ_y and σ_z are the Pauli matrices. Squaring the expression for the Hamiltonian we obtain

$$H_j{}^2 = \frac{\hbar^2}{4}\left(\Delta_j{}^2 + \Omega_0{}^2\right)\cdot\begin{pmatrix} 1 & 0 \\ 0 & 1 \end{pmatrix}$$

$$= \left(\frac{\hbar\Delta_j}{2}\sqrt{1+{x_j}^2}\right)^2 \cdot \mathbb{I} \ . \tag{A3}$$

With the above, we can obtain expressions for the Hamiltonian raised to arbitrary even and odd powers. Taking k to be an arbitrary integer we have

$${H_j}^{2k} = \left(\frac{\hbar\Delta_j}{2}\sqrt{1+{x_j}^2}\right)^{2k} \cdot \mathbb{I} \tag{A4}$$

and

$${H_j}^{2k+1} = \left(\frac{\hbar\Delta_j}{2}\sqrt{1+{x_j}^2}\right)^{2k+1} \cdot \frac{1}{\sqrt{1+{x_j}^2}}\begin{pmatrix} 1 & \alpha_j \\ {\alpha_j}^* & -1 \end{pmatrix} \tag{A5}$$

for the even and odd powers of the Hamiltonian, respectively, with $\alpha_j \equiv x_j \mathrm{e}^{-\mathrm{i}\varphi_j}$. With these expressions it is straightforward to calculate the matrix elements needed for the error calculation, beginning with evaluation in the ground state:

$$\begin{aligned} \langle 0|{H_j}^{2k}|0\rangle &= \left(\frac{\hbar\Delta_j}{2}\sqrt{1+{x_j}^2}\right)^{2k} \langle 0|\mathbb{I}|0\rangle \\ &= \left(\frac{\hbar\Delta_j}{2}\sqrt{1+{x_j}^2}\right)^{2k} \end{aligned} \tag{A6}$$

and

$$\begin{aligned} \langle 0|{H_j}^{2k+1}|0\rangle &= \left(\frac{\hbar\Delta_j}{2}\sqrt{1+{x_j}^2}\right)^{2k+1} \cdot \frac{1}{\sqrt{1+{x_j}^2}} \cdot \begin{pmatrix} 1 & 0 \end{pmatrix}\begin{pmatrix} 1 & \alpha_j \\ {\alpha_j}^* & -1 \end{pmatrix}\begin{pmatrix} 1 \\ 0 \end{pmatrix} \\ &= \left(\frac{\hbar\Delta_j}{2}\sqrt{1+{x_j}^2}\right)^{2k+1} \cdot \frac{1}{\sqrt{1+{x_j}^2}} \ . \end{aligned} \tag{A7}$$

Armed with these expressions we calculate the expectation value in the ground state of the unitary evolution operator for the j^{th} spin site:

$$\begin{aligned} \langle 0|U_j|0\rangle &= \left\langle 0\left| e^{-\frac{iH_j t}{\hbar}} \right| 0\right\rangle = \left\langle 0\left| \sum_{k=0}^{\infty} \frac{1}{k!}\left(-\frac{iH_j t}{\hbar}\right)^k \right| 0\right\rangle \\ &= \left\langle 0\left| \sum_{k=0}^{\infty} \left[\frac{1}{(2k)!}\left(-\frac{iH_j t}{\hbar}\right)^{2k} + \frac{1}{(2k+1)!}\left(-\frac{iH_j t}{\hbar}\right)^{2k+1}\right] \right| 0\right\rangle \\ &= \sum_{k=0}^{\infty} \frac{1}{(2k)!}\left(-\frac{it}{\hbar}\right)^{2k} \langle 0|H^{2k}|0\rangle + \sum_{k=0}^{\infty} \frac{1}{(2k+1)!}\left(-\frac{it}{\hbar}\right)^{2k+1} \langle 0|H^{2k+1}|0\rangle \\ &= \sum_{k=0}^{\infty} \frac{1}{(2k)!}\left(-\frac{it}{\hbar}\right)^{2k} \left(\frac{\hbar\Delta_j}{2}\sqrt{1+{x_j}^2}\right)^{2k} \end{aligned}$$

$$+\sum_{k=0}^{\infty}\frac{1}{(2k+1)!}\left(-\frac{it}{\hbar}\right)^{2k+1}\left(\frac{\hbar\Delta_j}{2}\sqrt{1+{x_j}^2}\right)^{2k+1}\cdot\frac{1}{\sqrt{1+{x_j}^2}}$$

$$=\sum_{k=0}^{\infty}\frac{1}{(2k)!}\left(-\frac{it\Delta_j}{2}\sqrt{1+{x_j}^2}\right)^{2k}+\sum_{k=0}^{\infty}\frac{1}{(2k+1)!}\left(-\frac{it\Delta_j}{2}\sqrt{1+{x_j}^2}\right)^{2k+1}\cdot\frac{1}{\sqrt{1+{x_j}^2}}$$

$$=\cosh\left(-\frac{it\Delta_j}{2}\sqrt{1+{x_j}^2}\right)+\frac{1}{\sqrt{1+{x_j}^2}}\sinh\left(-\frac{it\Delta_j}{2}\sqrt{1+{x_j}^2}\right)$$

$$=\cos\left(\tfrac{t\Delta_j}{2}\sqrt{1+{x_j}^2}\right)-\tfrac{i}{\sqrt{1+{x_j}^2}}\sin\left(\tfrac{t\Delta_j}{2}\sqrt{1+{x_j}^2}\right). \tag{A8}$$

The next step in deriving the error is to calculate the modulus squared of this matrix element, which is found to be:

$$\left|\langle 0|U_j|0\rangle\right|^2=\left|\cos\left(\frac{t\Delta_j}{2}\sqrt{1+{x_j}^2}\right)-\frac{i}{\sqrt{1+{x_j}^2}}\sin\left(\frac{t\Delta_j}{2}\sqrt{1+{x_j}^2}\right)\right|^2$$

$$=\cos^2\left(\frac{t\Delta_j}{2}\sqrt{1+{x_j}^2}\right)+\frac{1}{1+{x_j}^2}\cdot\sin^2\left(\frac{t\Delta_j}{2}\sqrt{1+{x_j}^2}\right)$$

$$=\frac{1+{x_j}^2\cos^2\left(\frac{t\Delta_j}{2}\sqrt{1+{x_j}^2}\right)}{1+{x_j}^2}\ . \tag{A9}$$

Finally, we obtain a closed-form expression for the exact value of the error on the control for the j^{th} spin site:

$$\epsilon_j=1-\left|\langle 0|U_j|0\rangle\right|^2$$

$$=1-\frac{1+{x_j}^2\cos^2\left(\frac{t\Delta_j}{2}\sqrt{1+{x_j}^2}\right)}{1+{x_j}^2}$$

$$=\frac{{x_j}^2\sin^2\left(\frac{t\Delta_j}{2}\sqrt{1+{x_j}^2}\right)}{1+{x_j}^2}. \tag{A10}$$

We now consider the case of the excited state. Using the above method it is straightforward to calculate that the expectation value in the excited state of the evolution operator is the complex conjugate of that in the ground state

$$\langle 1|U_j|1\rangle = \cos\left(\frac{t\Delta_j}{2}\sqrt{1+{x_j}^2}\right) + \frac{i}{\sqrt{1+{x_j}^2}}\sin\left(\frac{t\Delta_j}{2}\sqrt{1+{x_j}^2}\right).$$

and hence the error function is the same for both

$$\begin{aligned}\epsilon_j &= 1 - \left|\langle 1|U_j|1\rangle\right|^2 = 1 - \left|\langle 0|U_j|0\rangle\right|^2 \\ &= \frac{{x_j}^2 \sin^2\left(\frac{t\Delta_j}{2}\sqrt{1+{x_j}^2}\right)}{1+{x_j}^2}.\end{aligned} \tag{A10}$$

We can expand the exact expression for the error on spin site *j* in a Taylor series to obtain

$$\begin{aligned}\epsilon_j &= \frac{{x_j}^2 \sin^2\left(\frac{t\Delta_j}{2}\sqrt{1+{x_j}^2}\right)}{1+{x_j}^2} \\ &= \sin^2\left(\frac{1}{2}\right)\cdot {x_j}^2 + \left[\frac{1}{2}\sin\left(\frac{1}{2}\right)\cdot\cos\left(\frac{1}{2}\right) - \sin^2\left(\frac{1}{2}\right)\right]\cdot {x_j}^4 \\ &\quad + \frac{1}{16}\left[\cos^2\left(\frac{1}{2}\right) - 10\sin\left(\frac{1}{2}\right)\cdot\cos\left(\frac{1}{2}\right) + 15\sin^2\left(\frac{1}{2}\right)\right]\cdot {x_j}^6 + O\left({x_j}^8\right) \\ &\cong .229849\cdot {x_j}^2 - .0194811\cdot {x_j}^4 + .000658058\cdot {x_j}^6 + O\left({x_j}^8\right),\end{aligned}$$

where in this example we have taken $t\Delta_j = 1$. We see that, for small values of $x_j = \Omega_0/\Delta_j$, the error is indeed bounded by a value of order $O\left(\frac{{\Omega_0}^2}{{\Delta_j}^2}\right)$ as claimed in the text.

In the Figure 5 on the right below, we show the exact error as a function of Ω_0/Δ_j, the ratio of the Rabi frequency to the detuning frequency, over a range of values of $t\Delta_j$ (0.1, 1.0, 2.0, 5.0). In Figure 5 on the left below we show the surface values of the error function.

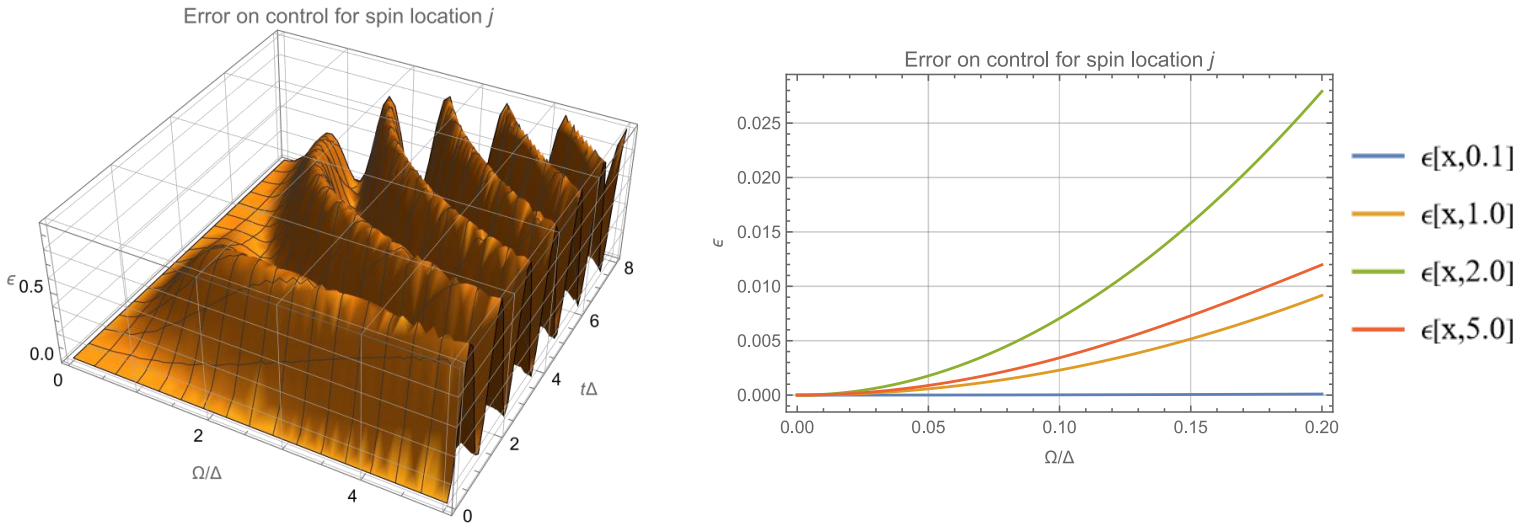

FIG. 5. Values of the error, given by equation A10. Left plot: Error as a function of Ω_0/Δ_j and $t\Delta_j$. Rabi oscillations occur along the $t\Delta_j$ axis. Right plot: Error for small Ω_0/Δ_j for several values of $t\Delta_j$. The error is bounded by a value of order $O\left(\frac{{\Omega_0}^2}{{\Delta_j}^2}\right)$.

2: Layer stack and dimensions for QMC and photonic chip

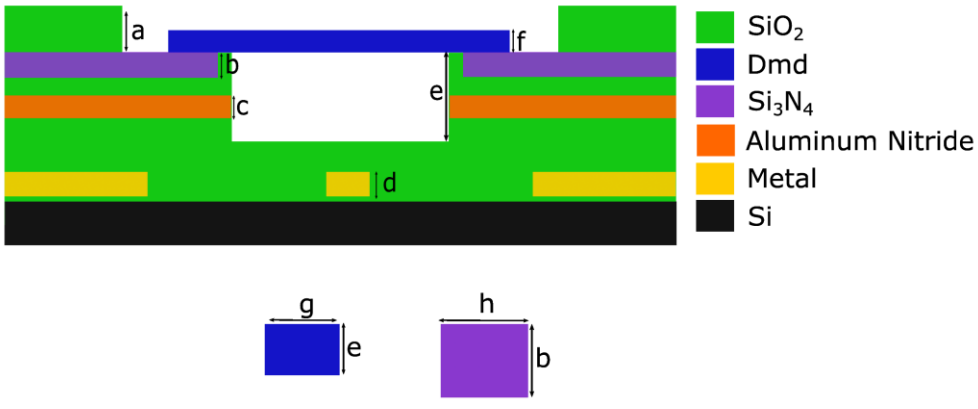

Dimension	a	b	c	d	e	f	g	h
Value (microns)	0.2	0.3	0.45	0.25	2	0.2	0.35	0.4

FIG. 6. Layer stack for the photonic chip and integrated diamond QMC.

Figure 6 shows a cross-section of the photonic chip with an integrated diamond QMC. We remove a section of the roughly 200 nm SiO2 cladding layer on the PIC, in order to create an optical coupling region where

the diamond waveguides can directly contact the SiN waveguides. We align the QMC and PIC during QMC placement. Aluminum traces connect to a narrow, 3 µm wide line running 2 µm beneath the QMC. Driving an AC current through this produces the AC magnetic field used to control the color center spins, yielding maximum field strength in the region of the QMC. A trench, etched in the center of the coupling region down to the aluminum wire, leaves the diamond waveguides suspended in air. This optimizes coupling between color center fluorescence and the fundamental optical mode in the waveguides, unperturbed by interactions with the substrate [1].

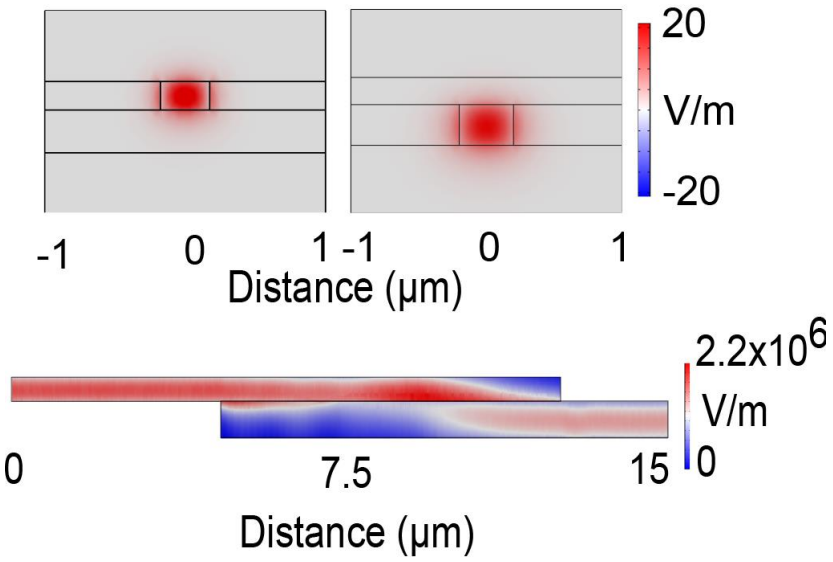

FIG. 7. Simulation of optical coupling between diamond and SiN waveguides.

Figure 7 shows a cross-section of the optical mode in the diamond waveguides (i), the SiN waveguides (ii), and the optical coupling between the QMC and SiN in the overlap region. Based on finite-element simulations, up to 95% optical coupling is achieved, assuming optimal alignment between the QMC and the PIC.

3: Microwave signal generation

For the spin control measurements in Section II, the output of a signal generator was amplified before being applied to the on-chip microwave line. The line was terminated off-chip by 50 ohms. The Rabi frequency was measured to be proportional to the square root of the applied microwave power (Fig. 8). This measurement was performed at a location in the QMC roughly 10 µm away from the microwave line.

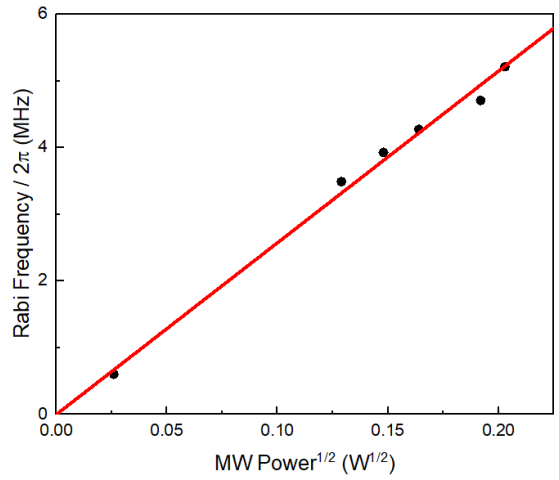

FIG. 8. Power dependence of the measured Rabi frequency.

For the frequency addressing demonstrated in Section III, a bias tee allowed a DC current to be applied on top of the microwave signal.

The microwave pulses used for the optimal spin control in Section IV were synthesized using a Xilinx Zynq Ultrascale+ RFSoC (radio frequency system-on-chip) on a ZCU111 Evaluation Board with an external trigger input. The RFSoC had a custom programmable logic design that stored pulses and released them when an external trigger was asserted to a high-speed complex mixer and multiplier, before sending them to the RFSoC DAC core. The RFSoC DAC core then mixed the signal to microwave frequencies around 2.9 GHz. This design enabled full control over the frequency, amplitude, and phase of the signal, allowing us to directly generate microwave pulses with the in-phase and out-of-phase amplitudes given in Fig. 5(a).

4: Additional ODMR and Rabi oscillation measurements

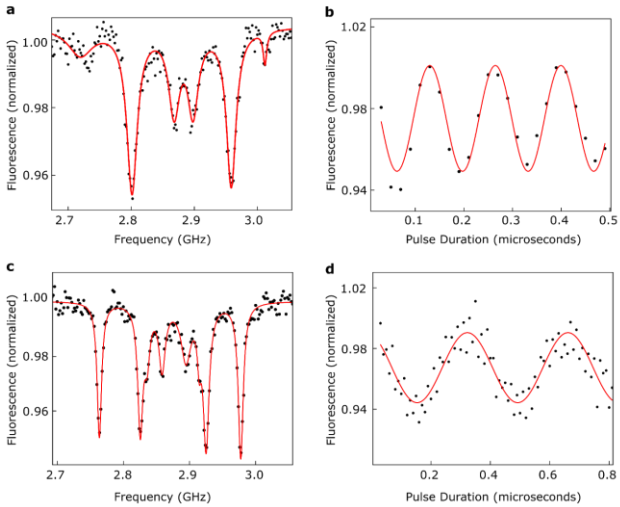

FIG. 9. ODMR and Rabi oscillation measurements. **a)** ODMR on channel 2. **b)** Rabi oscillations on channel 2. **c)** ODMR on channel 3. **d)** Rabi oscillations on channel 3.

Figure 9 shows additional ODMR and Rabi oscillation measurements for NV centers in channels 2 and 3 in the QMC as labeled in Fig. 3(d).

5: Additional spatially varying Zeeman shift measurements

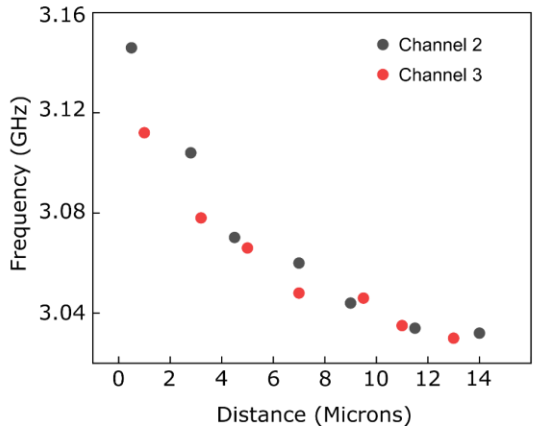

FIG. 10. Spatial dependence of transition frequency.

Figure 10 shows the transition frequency at 150 mA DC current for different locations in channels 2 and 3, used to construct the address map in Fig. 3(d).

6: Scalability of the selective control schemes

Experimentally the hyperfine coupling puts a major constraint on the number of spins that can be frequency resolved. Using Equation A10, we can calculate that to perform a π-rotation on a target NV spin independent of the nuclear spin state, with $\epsilon_i > 0.99$, (> 99% population in the excited state averaged over all three hyperfine states), requires $\Omega_0/2\pi > 17.8\ MHz$. Since ϵ_j is bounded from above by $(\Omega_0/\Delta_j)^2$, achieving $\epsilon_j < 0.01$ requires $\Delta_j/2\pi > 178\ MHz$. Given the total Zeeman shift shown in Fig. 3(b)ii, two hyperfine coupled NV spins could be frequency resolved using $I_{DC} = 150\ mA$. As demonstrated in Section IV, pulse shapes can be designed to achieve selective control of hyperfine coupled spins at much smaller Δ_j and with much lower peak Ω.

To further explore the scalability of our two approaches we now consider the simpler case of no hyperfine coupling. Experimentally this could correspond to cases where nuclear spins are initialized, or for color centers with much larger hyperfine splitting or not hyperfine coupling such as SnV [2]. For frequency resolved control, the lower limit on Ω_0, and therefore Δ_j, is now set by T_2. If we choose $\Omega_0/2\pi = 0.833\ MHz$ (π-pulse = 600 ns) and again require $\epsilon_j < 0.01$, then $\Delta_j/2\pi > 8.33\ MHz$.

However, in our device Ω_j has a spatial dependence as well as Δ_j. In Fig. 3(a,b) the simulated spatial dependence of $\vec{B}_{DC}$ and $\vec{B}_{AC}$ was used to calculate the spatial dependence of the state error for hyperfine coupled spins. We perform a similar calculation for several non-hyperfine coupled spins at different locations along the waveguide. The magnitude of $\vec{B}_{AC}$ is adjusted for each spin so that $\Omega_i/2\pi =$

0.833 MHz. We then map out the regions where $(\Omega_j/\Delta_j)^2 > 0.01$. The results, shown in Fig 11(a), indicate that as many as 17 spins could be frequency resolved in our device given $I_{DC} = 150\ mA$.

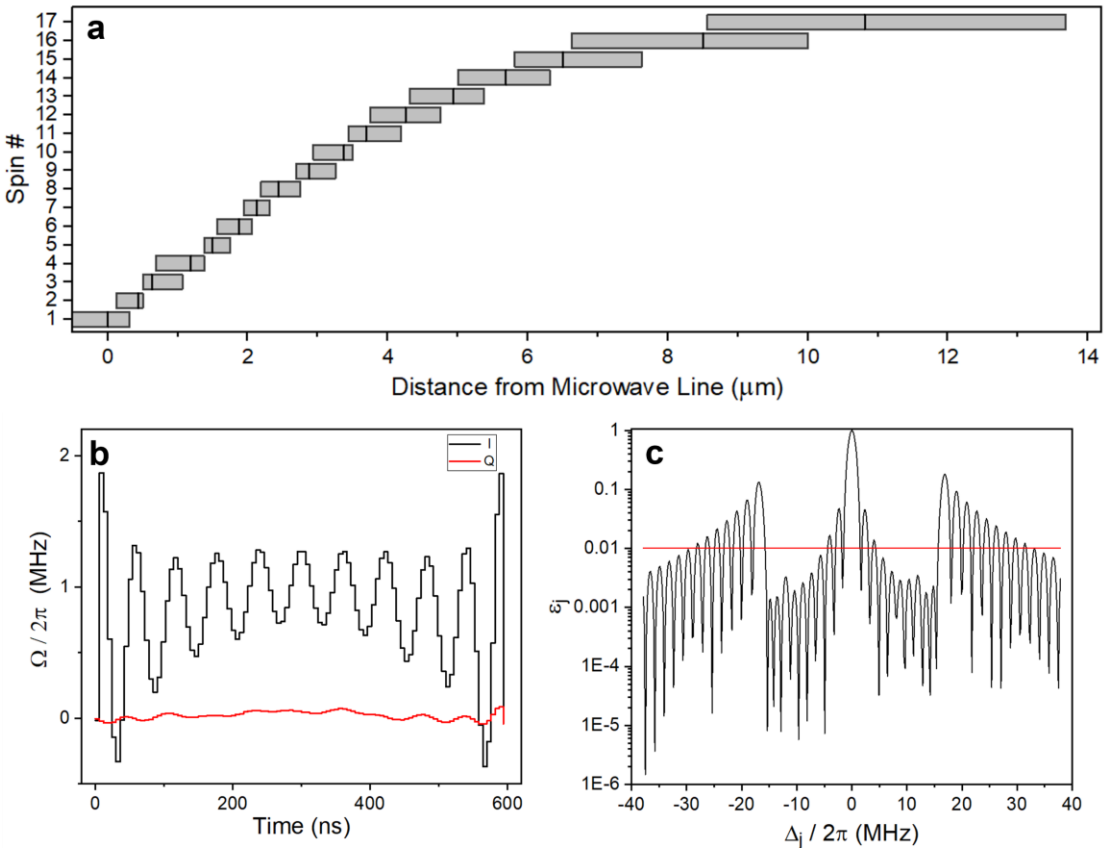

FIG. 11. (a) Frequency resolved control using rectangular pulses. Vertical lines indicate the location of each spin. Grey boxes indicate the region where the simulated $(\Omega_j/\Delta_j)^2 > 0.01$. Each spin location is selected such that it is outside this region for the two adjacent spins. **(b,c)** Optimized control with 21 spins. **(b)** Optimized pulse shape. **(c)** Simulated state error as a function of detuning from the target spin. The red line indicates the $\epsilon_j < 0.01$ threshold. The full detuning range shown here corresponds to locations between 1.25 μm and 4.5 μm away from the MW line.

Optimal control can offer an improvement in this case as well. To illustrate, we consider 21 spins equally spaced in frequency by only 1.5 MHz, and run the optimization code to perform a π-rotation on the center spin while returning all other spins to the ground state, limiting the pulse length to 600 ns. We again use the magnetic field simulations to calculate how Ω_j varies with Δ_j. Fig 11(b) and (c) show the resulting pulse shape and the calculated state error as a function of Δ_j when this pulse is applied. The optimized pulse succeeds at achieving $\epsilon_j < 0.01$ for all the spins. Note that while the optimization only considered Δ_j for each of the spins, Fig 11(c) indicates that the control pulse produces low crosstalk at other detunings as well.

7: Optimal control examples

The optimized pulse shape technique is useful beyond the special case of a π-rotation on a single target. To demonstrate the versatility of this tool we consider the case of 5 spins, equally spaced by 1.5 MHz, with a single control field tuned on resonance with the central spin. We then generate pulse shapes for producing various control schemes on all 5 spins. The calculated results, shown in Fig 12, indicate the possibility of performing control on subsets of spins, phase control, and arbitrary rotations.

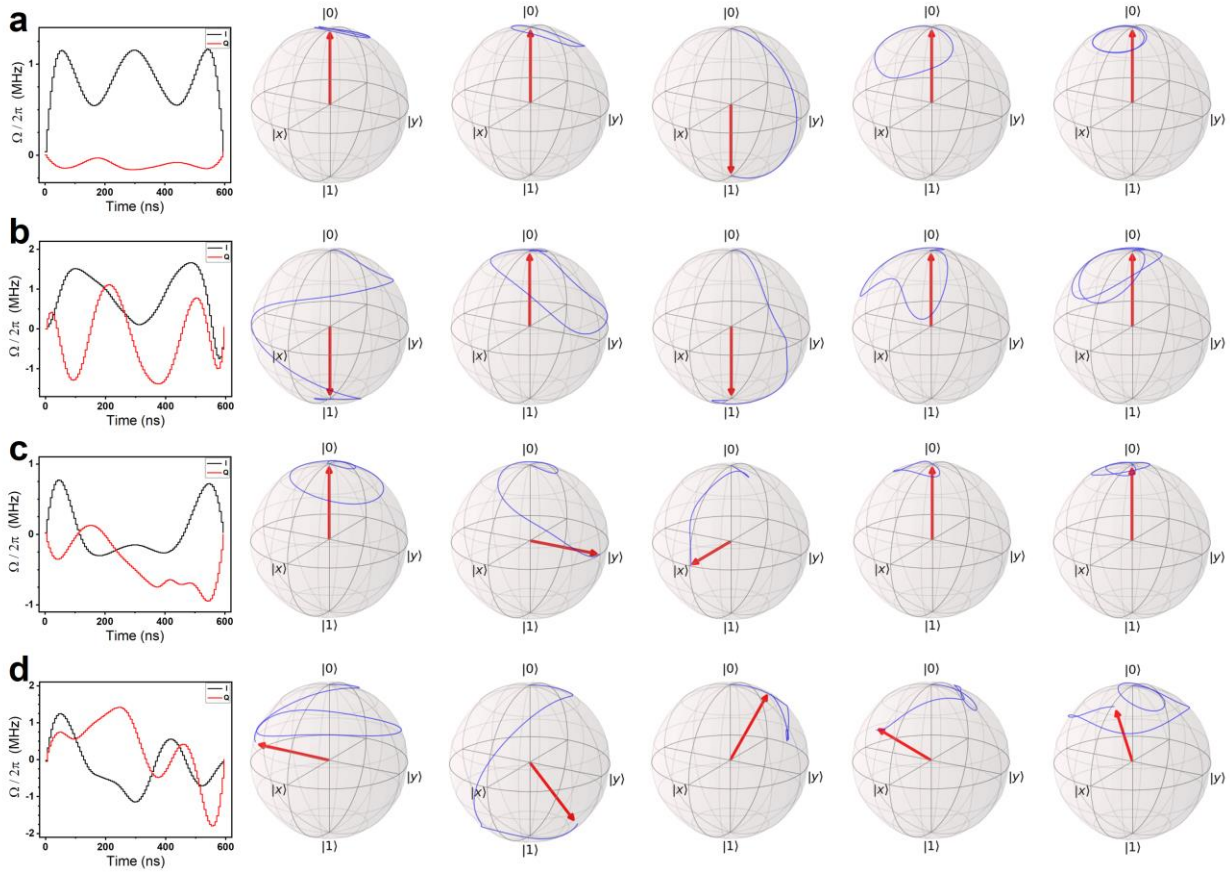

FIG. 12. Optimized control over 5 spins. **(a)** π-rotation on one spin. **(b)** π-rotation on two spins. **(c)** $\pi/2$-rotation on two spins with phase control. **(d)** Arbitrary rotations on all spins. Plots on the left indicate the pulse shape for achieving the desired control operation. All spins are initialized in $|0\rangle$. The red arrows indicate the desired final state on the Bloch sphere. The blue lines trace out the calculated path followed by the spin during the application of the control pulse. All spin rotations shown achieved a theoretical $\epsilon_j < 0.002$.

8: ODMR using the optimized pulse

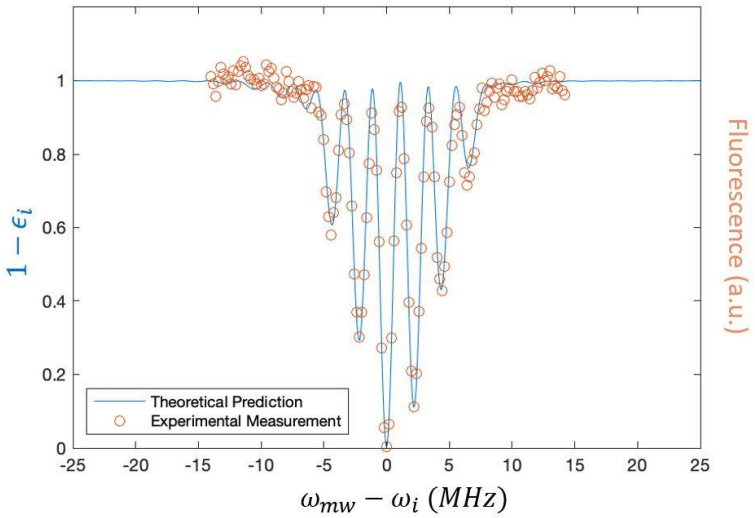

FIG. 13. ODMR using the optimally shaped pulse. Orange circles are experimentally measured fluorescence as a function of microwave frequency. The blue line is the theoretically calculated population in the ground spin state after the application of the optimal microwave pulse. The amplitude (y-axis scale) is taken as a fitting parameter.

To aid in the experimental calibration of the optimized microwave pulses shown in Fig. 4(a), we performed an ODMR measurement using these optimized pulses rather than the rectangular pulses that were used for ODMR in Fig. 2(a) and Fig. 3(c) inset. The good match, shown in Fig. 13, between theory (blue line) and experiment (orange circles) across the detuning range further confirms that we are reliably generating the optimized pulse shape and that the spin is undergoing the expected evolution during the application of the pulse. A detuning of zero corresponds to the conditions for the target spin. A detuning of 1.1 MHz corresponds to the conditions for the neighbor spin. Though for our purposes these are the only two frequencies that matter, the existence of multiple fringes in the ODMR indicates the potential for scaling selective control to many closely spaced spins.

[1] S. L. Mouradian et al., *Scalable Integration of Long-Lived Quantum Memories into a Photonic Circuit*, Phys. Rev. X **5**, 031009 (2015).

[2] R. Debroux et al., *Quantum Control of the Tin-Vacancy Spin Qubit in Diamond*, Phys. Rev. X **11**, 041041 (2021).